Effects of high pressure torsion on microstructures and properties of an $Al_{0.1}$CoCrFeNi high-entr opy alloy

P.F. Yu[a], H. Cheng[a], L.J. Zhang[a], H. Zhang[a], Q. Jing[a], M.Z. Ma[a], P.K. Liaw[b], G. Li[a,b*], and R.P. Liu[a**]

[a]State Key Laboratory of Metastable Materials Science and Technology, Yanshan University, Qinhuangdao 066004, China

[b]Department of Materials Science and Engineering, The University of Tennessee, Knoxville, TN 37996-2200, USA

[*]G. Li: email gongli@ysu.edu.cn; [**]R.P. Liu: email riping@ysu.edu.cn

Abstract

High pressure torsion (HPT) under a pressure of 6 GPa through 1 and 2 revolutions have been used to follow the evolution of microstructures and properties in an $Al_{0.1}$CoCrFeNi high-entropy alloy (HEA). The plastic-deformation mechanisms of the HEA include dislocation slip at low strains and twinning at high strains at room temperature. The planar dislocation slip on the normal face-centered-cubic slip system, {111}<110>, and nanoscaled deformation twins with a thickness from several nanometers to 40 nm, accompanied with some secondary twins. The hardness of the $Al_{0.1}$CoCrFeNi HEA increases from 135 Hv at hot-isostatic pressed (HIPed) state to about 482 Hv after HPT processing. The HEAs have a relatively high initial hardness and high work hardening, compared with traditional alloys. The creep resistance of the HEA processed by HPT was determined by a nanoindentation technique. The strain rate sensitivity, *m*, increases with the decreasing of grain size, for smaller

activation volume and the dominant deformation mechanism changing from the dislocation slip to grain-boundary slide. The present results give the plastic-deformation mechanism and mechanical properties evolution of single-phase HEA processed by HPT at room temperature.

Keywords: High-entropy alloy; High pressure torsion; Deformation twinning; Microhardness; Nanoindentation creep

1. Introduction

In the past decade, high-entropy alloys (HEAs) have attracted much research interest because of their unusual structural properties [1–3]. HEAs possess a highly-distorted lattice structure for the different atomic sizes and chemical bonds of the constituent elements [4]. Thus, the plastic-deformation mechanism of HEAs could be different from conventional alloys. The typical mechanisms of plastic deformation are by the slip of dislocations and twinning in conventional alloys [5]. While for the amorphous alloys, it is hard to define dislocations and twinning. A model of the shear-transition-zone (STZ) was proposed by Argon [6] and a model of free volumes by Spaepen [7]. However, for HEAs consisting of five or more elements in equiatomic proportions, Zhang et al. proposed that the plastic-deformation mechanism is believed to be just located in between the conventional alloys and the amorphous metals [6]. Zhu et al. studied the incipient plasticity and dislocation nucleation of the FeCoCrNiMn HEA by instrumented nanoindentation [8]. A mechanism consisting of a heterogeneous dislocation-nucleation process with vacancy-like defects (~ 3 atoms) as the rate-limiting nuclei appeared to be dominant.

Numerous methods, including tension, compression, rolling, forging, and torsion, could induce plasticity of HEAs. Some studies of rolled and recrystallized single-phase HEAs: one in which room-temperature hardness was investigated as a function of grain size [9] and the other in which preliminary tensile tests were performed at different temperatures [10]. Otto et al. [11] studied the tensile behavior of a face-centered-cubic (FCC) crystal-structured CoCrFeMnNi HEA in the temperature range between 77 K (-196 °C) and 1,073 K (800 °C). They found that the initial plasticity, up to the tensile strain of about 2%, occurs exclusively by the planar glide of 1/2 <110> dislocations on {111} planes in the temperature range of 77 – 873 K (-196 – 600 °C). Upon lowering the test temperature from room temperature to 77 K, nanoscaled twinning was observed as an additional deformation mode in specimens interrupted after strains of 20% or more. The mechanical properties of HEAs actually improve at cryogenic temperatures for a transition from the planar-slip dislocation activity at room temperature to deformation by mechanical nanotwinning with decreasing temperature, which results in the continuous steady strain hardening [12].

So far, few studies focus on the influence of the shear stress on HEAs. A high-pressure-torsion (HPT) technique could introduce the strong shear stress. It is used over the last several decades to refine the microstructure or study the plastic-deformation mechanism of crystalline alloys. Recently, the mechanical properties, microstructure and thermal stability of CoCrFeMnNi HEA after HPT were studied [13], whereas the deformation mechanisms and the creep behavior were not

examined deeply. Our goal here was to study the plastic-deformation mechanism, microstructure, and property evolution of a representative single FCC solid-solution phase, $Al_{0.1}$CoCrFeNi HEA processed by HPT. To link mechanical changes with the microstructure, transmission electron microscope (TEM) was used, which is capable of visualizing the structure evolution along the radius of the sample to explain the relationship among the plastic-deformation mechanism, mechanical properties, and the shear strain. After HPT processing, the HEAs become graded materials along the radius with different grain size. The hardness and creep-resistance property are different along the radius, which were tested by Vickers hardness tester and nanoindentation, respectively. The clarification of the plastic-deformation mechanism and properties evolution of the FCC structure HEAs provide a theoretical basis for the applications of the HEAs.

2. Methods

The target alloy used in the present work has the nominal composition of $Al_{0.1}$CoCrFeNi (in atomic proportion). The alloys were prepared by arc-melting a mixture of the constituent elements with purity better than 99.9 weight percent (wt.%) in a Ti-gettered high-purity argon atmosphere. Repeated melting was carried out at least five times to improve the chemical homogeneity of the alloy. Then, the master alloy melt was casted as a ~130 × 300 × 20 mm^3 plate by vacuum induction. The plate was hot-isostatic pressed (HIPed) at 1,473 K (1,200 °C), 100 MPa for 4 hours. Argon gas was used to supply a high pressure (100 MPa) during the HIPed process. The HIPed samples were then placed in a horizontal tube furnace with high purity argon at

1,423 K for 50 hours.

The as-HIPed samples were sectioned into pieces (Φ 10 mm × 1.0 mm) by electric-discharge machining. Then, the samples were compressed at 6 GPa through 1 and 2 turns with the rotation speed of 1 revolution/minute. Using above measured parameters, the equivalent von Mises strain (ε) is obtained by the following equation [14]:

$$\varepsilon = \frac{2}{\sqrt{3}} \ln \left[\left(1 + \frac{\gamma^2}{4} \right)^{\frac{1}{2}} + \frac{\gamma}{2} \right] \quad (1)$$

and the total shear deformation imposed strain (γ) as a function of the distance from the center of disk (r) is given by [14]:

$$\gamma = \frac{2\pi N r}{h} \quad (2)$$

where N indicates the number of torsion for 360º; and h represents the thickness of the disk. After HPT processing, the plates were cut to 5 small pieces with 2 × 2 mm along the diameter. The structure of each pieces near center was detected by X-ray diffraction (XRD) using a D/MAX-2500/PC diffractometer with the Cu Kα radiation (λ = 1.54 Å) from 20° to 100° of 2θ with 2°/min. The working voltage and current are 40 kV and 100 mA, respectively. For the metallographic observation, the sample surface was sequentially polished down to 0.1-μm diamond abrasion paste finish and, then, etched with an aqua regia solution. The TEM specimens of the HPT sample were prepared by dimpling and ion-beam milling with a low-energy ion beam to avoid being damaged. The TEM observations were performed at 200 kV in a JEM-2010 microscope for the bright-field (BF) image, dark-field (DF) image,

select-area electron diffraction (SAED), and high-resolution TEM (HRTEM) investigations. The inverse fast Fourier transform (IFFT) algorithm was acquired from HRTEM to analyze the structure of the specimen.

After processing by HPT, the 10-mm discs were polished to a mirror-like surface, and the Vickers microhardness was measured with an applied load of 300 g for 10 s along the radii from the center to edge at different radial directions. Nano-indentation experiments were conducted on a nanoindenter Hysitron TriboIndenter with a diamond Berkovich tip having a 260 nm radius of the curvature [15]. The load was increased up to the maximum load, P_{max}, of 4,000 μN at a loading rate of 400 μN/s. The indenter was held at P_{max} for 10 s to measure the time-dependent displacement, and the unloading kept the same rate as the loading rate. The data were gained from the center to edge for an interval of 2 mm and averaged in groups of five.

3. Results

3.1 Microstructural evolution during HPT

Figure 1 shows the XRD profiles for the edge of the $Al_{0.1}CoCrFeNi$ HEA samples that are HIPed and subjected to HPT processing at 6 GPa for $N = 1$ and 2 (r = 4 mm, $\varepsilon_{N=1} \approx 3.72$, and $\varepsilon_{N=2} \approx 4.52$), respectively. All the XRD curves indicate a single FCC solid-solution phase without the phase transition after HPT processing. However, the diffraction peaks broaden during the HPT processing. The diffraction peaks broadening were caused by the lattice strain and the grain size decreasing with the increasing of shear strain. The lattice strain of the samples calculated by XRD data are 0.09% (as-HIPed), 0.18% (N = 1), and 0.52% (N = 2), respectively. Meanwhile,

the intensities of diffraction peaks decrease with the increasing of shear strain. The variation of XRD peak intensities is similar to that caused by the addition of multi-principal elements with different atomic sizes [16]. High pressure and shear strain could increase the lattice strain resulting in the significant loss of crystallization perfection and the severe X-ray scattering effect, which is responsible for the decreasing of the peak heights.

HEAs possess a highly-distorted lattice structure, inducing its high hardness and strength [17]. After the HPT processing, the lattice distortion becomes larger according to the peaks broadening and the deceasing of peak heights. Thus, the processing of HPT could impact the hardness and strength of HEAs for high shear strains, which can be confirmed by Vickers microhardness test results, as discussed below. The variation of the grain size was characterized by the optical micrograph and the TEM images.

The grain size in the material prior to HPT was close to several millimeters according to the optical micrograph in Fig. 2a. From the BF TEM image in Fig. 2d, some clear and wiggled dislocation lines could be seen in the $Al_{0.1}$CoCrFeNi HEA. The [100] direction diffraction pattern inserted in Fig. 2d indicates the FCC phase of the $Al_{0.1}$CoCrFeNi HEA. After being processed by HPT at 6 GPa through 1 revolution, the grain of the HIPed sample transforms from the micrometer-sized coarse grain to strip structure (with a grain width of nearly 100 μm) along the direction of the shear strain and some fine structure shown in Fig. 2b. The fine area was represented by the BF TEM image and diffraction pattern in Fig. 2e. There is some fraction of coarse

grains with rugged and fuzzy boundaries. The dislocation-density increase and dislocation tangling will result in work hardening after HPT. The corresponding SAED pattern is, logically, formed by incomplete rings. Further increasing the processing strain level to 2 revolutions in HPT yielded the formation of a nanocrystalline structure throughout the disk. It cannot distinguish obvious grain boundaries on the optical micrograph in Fig. 2c. Figure 2f shows a typical homogeneous nanocrystalline distribution with grain sizes of about 80 nm near the edge of the 2-revolution HPT disk. Thus, the SAED patterns corresponding to the edge regions of the samples through HPT by applying a pressure of 6 GPa for two revolutions are formed by complete rings (Fig. 2f inserted).

3.2 Dislocations and twins in the $Al_{0.1}$CoCrFeNi HEA

Figure 3 is a TEM BF micrograph showing the typical dislocation structure in the coarse grain material after HPT processed at 6 GPa through 2 revolutions. For the grains in the center of the sample, two directions' glide lines are perpendicular to $(11\bar{1})$ and $(\bar{1}\bar{1}1)$ planes according to the [110] orientation-diffraction pattern shown in Fig. 3a, respectively, demonstrated by the trace analysis. Therefore, the dislocation glide of the plastic deformation of the $Al_{0.1}$CoCrFeNi alloy is strongly localized on a distinct set of {111}-type FCC lattice planes. This trend is in line with earlier studies, which investigated the dislocation plasticity in the concentrated binary FCC solid solutions [18–21]. The grains in the edge of the sample with high strains (see Fig. 3b), the dislocation structure has changed to dislocation cells from the planar dislocation glide at low strains. The cell sizes are in the range of 100 – 200 nm.

The bright and dark field images, the corresponding diffraction pattern, and HRTEM images shown in Fig. 4 reveal extensive deformation twinning in the $Al_{0.1}$CoCrFeNi HEA deformed by HPT (6 GPa, N = 2) at room temperature. The deformation twins with a thickness from several nanometers to 40 nm were presented in Fig. 4a (BF TEM) and Fig. 4c (DF TEM). The corresponding SAED pattern (the matrix axis is $[011]_M$, and the twin axis is $[\bar{0}\bar{1}\bar{1}]_T$) is shown in Fig. 4b, demonstrating that these inside nanoscaled twins belong to the phase with an FCC structure and a {111} twin plane. The HRTEM image in Fig. 4d focuses on a region in which four deformation twins with a thickness of about several nanometers cross the field of the observation. Twinning planes and the twin boundary are indicated by red and black straight lines, respectively (Fig. 4d). Therefore, twinning is another plastic deformation mode for the $Al_{0.1}$CoCrFeNi HEA processed by HPT at room temperature.

In some areas of the sample, secondary twins could be found, shown in Fig. 5. Figure 5a shows primary twins running from the top left to bottom right (red arrows), and secondary twins in inclined orientations (blue arrows). The SAED patterns, including the matrix, primary and secondary twins are shown in Fig. 5b. The diffraction patterns of the matrix, primary and secondary twins are indicated by white, red, and blue parallelograms, respectively, in Fig. 5b. Figure 5c is the corresponding DF image, which shows obvious primary twins and needlelike secondary twins. Figure 5d presents an HRTEM image on the formation behavior of twin junctions when secondary twins (indicated by blue lines) penetrate the primary twins (indicated

by red lines). In the initial stage of plastic deformation, primary twins were induced by the shear stress in HPT. Secondary twins appear later. Meanwhile, secondary twins and dislocations are constrained by primary twins efficiently. It is obvious that deformation twinning will lead to work hardening during plastic deformation by serving as effective barriers for the secondary twins and dislocation movements. This trend is similar to the twinning-induced plasticity steel processed by HPT [22]. Microstructures of the HEAs show obvious change after HPT processing according to the XRD and TEM results, including the dislocation increasing, grain refinement, and twinning along the radius, which will change the hardness and creep-resistance property. Therefore, the microhardness and creep behavior were examined by the Vickers hardness tester and nanoindentation.

3.3 Microhardness measurements across the disk diameters after HPT

We plot the values of Vickers microhardness, Hv, against the distance from the disk centers for two testing conditions, as shown in Fig. 6 for 1 and 2 revolutions, respectively. For each condition, the values of Hv are tested for three times along the radii from the center to edge at different radial directions. The data were averaged and their standard deviations used as an indicator of the error. The microhardness is improved after being processed by HPT. The average Vickers microhardness of the HIPed sample is 135 Hv. After 1 revolution, the hardness begins to saturate at the edge. After 2 revolutions the hardness reaches a saturation state with a hardness about 482 Hv at a radius of about 3 mm from the center and extends to the outer edge of the disk. These results agree with the microstructure of the samples processed by HPT

indicating a saturation in grain refinement. The distribution of hardness after HPT depends on the material and various physical factors [13]. For pure aluminum [23], there is a region of higher hardness up to Hv ≈ 50 between the center and the edge, and this region of higher hardness reaches a maximum at ~ 2.5 mm from the center of the disk for N = 1/4 turn.

3.4 Nanoindentation tests

The plastic deformation appears when the stress exceeds elastic limit stress. While, the creep could appear as the time long enough even the stress is less than the elastic limit. In another word, creep is another important deformation mode. The plates of HEAs after processing by HPT are graded materials along the radius with different grain size. The creep behavior is different along the radius. The nanoindentation method has been widely used for the study of mechanical properties and deformation behavior in a small volume of materials, particularly the study of rate-dependence processes such as nanoindentation creep. Therefore, except for hardness, the creep behavior was studied by nanoindentation from the center to edge of the HEA processed by HPT through 2 revolutions. Figure 7a shows the load vs. displacement ($P - h$) curves at the points of different distances from the disc center (r = 0 mm, 3 mm, and 5 mm) composed of the loading and unloading parts. These curves overlapped each other below 20 nm. Then, they deviate from one another, and displacements increase from the center to edge. The variations in the creep depth at different points are displayed in Fig. 7b during the holding period as a function of time in the nanoindentation-creep tests. Creep curves include the initial stage known

as the transient creep, and the later corresponding to the steady-state creep. The creep depth increases from 4.12 to 12.08 nm from the center (r = 0 mm) to the edge (r = 5 mm). The indentation depth is also found to be influenced by the distance from the center: the slope of the line becomes steeper near the edge.

To further illustrate the creep behavior of HEAs processed by HPT, the strain rate sensitivity (SRS), m, was calculated by plotting ln$H$ versus the ln$t$, where H is the hardness, and t is the time.

The indentation creep rate, $\dot{\varepsilon}$, stress, σ, and temperature, T, are usually correlated via an empirical power-law creep equation [24]

$$\dot{\varepsilon} = a\sigma^{\frac{1}{m}} \exp(-Q/RT) \tag{3}$$

Following the earlier investigators [25], the relationship between the strain rate and hardness (H) gradient can be determined as

$$\dot{\varepsilon} = -\beta \frac{1}{H}\frac{dH}{dt} \tag{4}$$

where β represents a constant, and the relation between the stress (σ) and hardness (H) could be described as

$$H = C\sigma \tag{5}$$

where C is a constant. Substituting Eqs. (4) and (5) into Eq. (3) and integrating the two sides of t, the relationship between the hardness of creep and the holding time is presented as follows:

$$-\frac{1}{m}\ln H = \ln B - Q/RT + \ln t \tag{6}$$

Then, ln$H$ is taken as the horizontal ordinate, and ln$t$ as the vertical ordinate, as demonstrated in Fig. 8. The SRS, m, is 0.012, 0.024, and 0.035 for r = 0, 3 mm, and 5

mm, respectively.

4. Discussion

4.1 Deformation mechanisms in the $Al_{0.1}$CoCrFeNi HEA

At the center of the sample, the strain is low. Therefore, dislocation slip was found to be strongly localized (planar) within a limited set of {111}-type slip planes which can be seen from Fig. 3a. With increasing the strain, the dislocations lose their planar character and transform to dislocation cells in Fig. 3b. Therefore, planar slip vanishes gradually, and the dislocations tend to arrange in a form that is more commonly found at low temperatures in pure FCC metals, such as Cu [21].

The emergence of deformation twinning during plastic deformation is correlated with many intrinsic and extrinsic factors, including the crystal structure, chemical composition, stacking fault energy (SFE) [26,27], strain rate [28], and temperature [11]. For HEAs, with multiple-element atoms constructing a distortion structure, SFE will be lower than the traditional alloys [29]. Meanwhile, lattice parameters becoming larger (demonstrated by XRD in Fig. 1) will also reduce SFE after being processed by HPT. Low SFE favors the production of deformation twinning. However, there is no deformation twinning when specimens are deformed at room temperature in the CoCrFeMnNi HEA subjected to by cold rolling [11], while extensive deformation twins are formed in the fine-grained (FG) specimen deformed to a plastic strain of 20.2% at 77 K (-196 °C) [11]. It demonstrates that the stress that is needed to induce deformation by twinning can be reached when specimens are deformed at low temperatures for the SFE will reduce with the temperature decreasing. However, in

our present work, HPT is a kind of severe plastic deformation method. The strain level is higher than the threshold of twin occurrence in the $Al_{0.1}$CoCrFeNi HEA at room temperature, resulting in twinning formation after HPT.

Twinning is expected to contribute to the increased work hardening by the introduction of new interfaces, which effectively reduces the dislocation mean free path and causes strengthening [30–34]. It is commonly referred to as the "dynamic Hall–Petch" effect. Very recently, our laboratory produces the hardest material in the world, which is a nanotwinned diamond [35]. It means that twins improve hardness efficiently in materials. Thus, twins will play similar effects on the hardness in HEAs.

The generation of secondary twins in the $Al_{0.1}$CoCrFeNi HEA can be substantially enhanced without sacrificing ductility [22]. The different twinning systems will be activated during subsequent deformation and lead to the simultaneous high strength, high ductility, and high strain hardening. This phenomenon will be more evident when temperature becoming lower [12]. Therefore, twinning is an important deformation mode in HEAs with an FCC structure.

We could conclude that the plastic deformation of the $Al_{0.1}$CoCrFeNi HEA with an FCC structure includes dislocations sliding and dislocation cells (Fig. 3) and deformation twinning (in Fig. 4) at room temperature, even some secondary twins are observed in Fig. 5.

4.2 The variation in microhardness

For most of alloys, the microhardness increases with increasing the strain (from the disc center to edge) after HPT processing, and saturates to a steady state at high

strains where the hardness remains unchanged with further straining. It was considered that the saturation stage (steady state) appears because of a balance between hardening and softening, where hardening is due to the dislocation accumulation and grain refinement, whereas softening is due to the annihilation of dislocations through recovery [36,37] or recrystallization [38,39]. For HEAs, the lattice distortion reduced for the increased lattice parameter also leads to the decreased microhardness (softening).

In order to compare the work hardening rate after HPT, we process the $Al_{0.1}CoCrFeNi$ HEA with 5 turns at 6 GPa, and the microhardness reaches the saturation value at 482 Hv on the periphery of the samples (Fig. 6). The effect of HPT on microhardness, Hv, was summarized in Fig. 9 for some pure metals and alloys [23,40–56]. The horizontal ordinate is the microhardness in the annealing state, Hv_0, and $\Delta Hv/Hv_0$ was plotted as the vertical ordinate. Where $\Delta Hv = Hv - Hv_0$, Hv is the saturation microhardness after being processed by HPT. The effect of HPT on materials could be divided into the hardening and softening behavior. For most of the pure metal and alloy, HPT induces dislocations [23], twinning [45], and grain refinements. The microhardness, Hv, increases with the equivalent strain and reaches saturation at a specific strain. However, for some pure metals, such as Pb, Zn, Sn, and In [46], the hardness level at the steady state attained by HPT decreases below the hardness level of the annealed sample prior to HPT. This trend may be due to the contribution of grain boundaries acting as a dislocation sink or causing grain-boundary sliding to release strain hardening [46]. For the Zn-22% Al alloy [56],

softening is due to a significant reduction of Zn precipitates during processing. Metallic glasses show evident softening, for the increased free volume after being processed by HPT [48, 49].

$\Delta Hv/Hv_0$ represents hardening or softening rates. The larger absolute value of $\Delta Hv/Hv_0$ indicates the more evident hardening or softening (Fig. 9). It can be concluded that most of the metals with an FCC structure have low initial microhardness and high work hardening. However, HEAs with an FCC structure have not only a relative high microhardness in the annealing state, but also high work hardening for their low SFE [29].

4.3 Creep behavior

The SRS, *m*, increases along the radius of the HEA plate from 0.012 to 0.035. In order to clarify the trend, the activation volume v^*, which is indicative of the number of atoms involved in the deformation process can be estimated based on the SRS and shear stress [57],

$$v^* = \frac{3\sqrt{3}kT}{mH} \tag{7}$$

where *k* is the Boltzmann constant, *T* is the absolute temperature in test, *H* is the hardness of the sample. Accordingly, the activation volume v^* was obtained as 0.89 nm^3, 0.28 nm^3, and 0.09 nm^3 for r = 0, 3 mm, and 5 mm, respectively. It turned out that the activation volume of the $Al_{0.1}CoCrFeNi$ HEA decreases with the grain size *d* reducing, which is accordance with other FCC structure materials. The smaller the activation volume, the easier the nucleation of the dislocation events. It is well know that self-diffusion, dislocation, and grain boundary are the most effective diffusion

paths under creep deformation. For nanocrystalline metals, the creep behavior may be dominated by grain-boundary sliding, grain-boundary diffusion, grain rotation, and dislocation climb [58]. At the center of the sample processed by HPT, the grain is coarse. The influence of grain boundaries on the SRS is very limited. Matsunaga *et al.* [59] investigated the intragranular deformation mechanism during room-temperature creep in a pure magnesium and found that the dominant deformation mechanism was the planar dislocation slip within the grain. Similar to the pure magnesium, the deformation mechanism at the center of the HEA is the dislocation slip, leading to a lower SRS. With increasing the shear stress, the role of the grain boundary in affecting the creep behavior becomes more and more remarkable for the grain refinement. The dominant deformation mechanism at the grain boundary was the grain-boundary gliding due to the high diffusion rate of the grain boundary. The SRS, *m*, increases from 0.012 at the center to 0.035 on the edge for the smaller activation volume and grain-boundary sliding with the decreasing of grain size. Therefore, the creep-resistance property of the $Al_{0.1}$CoCrFeNi HEA reduces along the radius of the plate after HPT processing.

5. Summary and conclusions

Processing by HPT produces a very substantial grain refinement in HEAs. The deformation mechanisms include dislocation slip and twinning at room temperature. The planar dislocation slip is on the normal FCC slip system, {111}<110>, and nanoscaled deformation twins with a thickness from several nanometers to 40 nm accompanied with some secondary twins. Twinning is an important deformation

mechanism for HEAs. After HPT, the microhardness reaches to a saturation value about 482 Hv at the edge of the sample for the balance between softening and hardening. The FCC structure HEAs with lower SFE have a high work hardening rate, compared with traditional alloys. The creep resistance of HEAs processed by HPT was determined by a nanoindentation technique. The SRS decreases with the strains increasing for the smaller activation volume and dominant deformation changing from the dislocation slip to grain-boundary sliding leading to a lower creep-resistance of the $Al_{0.1}$CoCrFeNi HEA.

Acknowledgments

The research was supported by the National Science Foundation of China (Grant No. 51271161/51171163/51121061). Gong Li would like to acknowledge the Specialized Research Fund for the Doctoral Program of Higher Education (Grant No. 20131333110019). Peter K. Liaw would like to acknowledge the U.S. Army Research Office project (W911NF-13-1-0438), the National Science Foundation (CMMZ-1100080) (Dr. S. N. Mathaudhu, Dr. D. Stepp, and Dr. C. Cooper as program directors) and the Department of Energy, Office of Fossil Energy, National Energy Technology Laboratory (DE-FE-0008855, DE-FE-0011194, and DE-FE-0024054), with Mr. V. Cedro, Mr. S. Markovich, Mr. R. Dunst, and Dr. J. Mullen as program managers, respectively.

References

[1] J.W. Yeh, Y.L. Chen, S.J. Lin, S.K Chen, Mater. Sci. Forum. 560 (2007) 1–9.

[2] L.J. Santodonato, Y. Zhang, M. Feygenson, C.M. Parish, M.C. Gao, R.J. Weber,

C.J. Neuefeind, Z. Tang, P.K. Liaw, Nat. Commun. 6 (2015) 5964-1–13 .

[3] Y. Zhang, T.T. Zuo, Y.Q. Cheng, P.K. Liaw, Sci. Rep. 3 (2013) 1455-1–7.

[4] J.W. Yeh, S.J. Lin, T.S. Chin, J.Y. Gan, S.K. Chen, T.T. Shun, C.H. Tsau, S.Y Chou, Metall. Mater. Trans. A 35A (2004) 2533–2536.

[5] Y. Zhang, T.T. Zuo, Z. Tang, M.C. Gao, K.A. Dahmen, P.K. Liaw, Z.P. Lu, Prog. Mater. Sci. 61 (2014) 1–93.

[6] A.S. Argon, Acta Metall. 27 (1979) 47–58.

[7] E.P. Barth, F. Spaepen, R. Bye, S.K. Das, Acta Mater. 45 (1997) 423–428.

[8] C. Zhu, Z.P. Lu, T.G. Nieh, Acta Mater. 61 (2013) 2993–3001.

[9] W.H. Liu, Y. Wu, J.Y. He, T.G. Nieh, Z.P. Lu, Scripta Mater. 68 (2013) 526–529.

[10] A. Gali, E.P. George, Intermetallics 39 (2013) 74–78.

[11] F. Otto, A. Dlouhý, C. Somsen, H. Bei, G. Eggeler, E.P. George, Acta Mater. 61 (2013) 5743–5755.

[12] B. Gludovatz, A. Hohenwarter, D. Catoor, E.H. Chang, E.P. George, R.O. Ritchie, Science 345 (2014) 1153–1158.

[13] B. Schuh, F. Mendez-Martin, B. Völker, E.P. George, H. Clemens, R. Pippan, A. Hohenwarter, Acta Mater. 96 (2015) 258–268.

[14] A.P. Zhilyaev, T.G. Langdon, Prog. Mater. Sci. 53 (2008) 893–979.

[15] W.C. Oliver, G.M. Pharr, J. Mater. Res. 7 (1992) 1564–1583.

[16] J.W. Yeh, S.Y. Chang, Y.D. Hong, S.K. Chen, S.J. Lin, Mater. Chem. Phys. 103 (2007) 41–46.

[17] W. Guo, W. Dmowski, J.Y. Noh, P. Rack, P.K. Liaw, T. Egami, Metall. Mater.

Trans. A 44 (2013) 1994–1997.

[18] V. Gerold, H.P. Karnthaler, Acta Metall. 37 (1989) 2177–2183.

[19] H. Neuhaüser, Acta Metall. 23 (1975) 455–462.

[20] J. Olfe, H. Neuhäuser, Phys. Status Solidi A 109 (1988) 149–160.

[21] P. Landau, R.Z. Shneck, G. Makov, A. Venkert, MRS Proc. 982 (2006) 0982-KK09-05.

[22] Y.J. Wei, Y.Q. Li, L.C. Zhu, Y. Liu, X.Q. Lei, G. Wang, Y.X. Wu, Z.L. Mi, J.B. Liu, H.T. Wang, H.J. Gao, Nat. Commun. 5 (2014) 1–8.

[23] M. Kawasakia, R.B. Figueiredo, T.G. Langdon, Acta Mater. 59 (2011) 308–316.

[24] W.B. Li, J.L. Henshall, R.M. Hooper, K.E. Easterling, Acta Metall. Mater. 39 (1991) 3099–3110.

[25] M.J. Mayo,W.D. Nix, Strength of Metals and Alloys, Pergamon, Oxford, 1988.

[26] L. Rémy, A. Pineau, Mater. Sci. Eng. 26 (1976) 123–132.

[27] A. Rohatgi, K.S. Vecchio, G.T. Gray, Metall. Mater. Trans. A 32 (2001) 135–145.

[28] J.W. Christian, S. Mahajan, Prog. Mater. Sci. 39 (1995) 1–157.

[29] A.J. Zaddach, C. Niu, C.C. Koch, D.L. Irving, JOM 65 (2013) 1780–1789.

[30] H. Beladi, I.B. Timokhina, Y. Estrin, J. Kim, B.C.D. Cooman, S.K. Kim, Acta Mater. 59 (2011) 7787–7799.

[31] U.I. Gutierrez, D. Raabe, Acta Mater. 59 (2011) 6449–6462.

[32] K.S. Raghavan, A.S. Sastri, M.J. Marcinkowski, Trans. Met. Soc. AIME 245 (1969) 1569–1575.

[33] I. Karaman, H. Sehitoglu, A.J. Beaudoin, Y.I. Chumlyakov, H.J. Maier, C.N. Tomé, Acta Mater. 48 (2000) 2031–2047.

[34] O. Bouaziz, N. Guelton, Mater. Sci. Eng. A 246 (2001) 319–321.

[35] Q. Huang, D.L. Yu, B. Xu, W.T. Hu, Y.M. Ma, Y.B. Wang, Z.S. Zhao, B. Wen, J.L. He, Z.Y. Liu, Y.J. Tian, Nature 501 (2014) 250–255.

[36] H.P. Stüwe, Acta Metall. 13 (1965) 1337–1342.

[37] M. Zehetbauer, Acta Metall. Mater. 41 (1993) 589–599.

[38] T. Hebesberger, H.P. Stuwe, A. Vorhauer, F. Wetscher, R. Pippan, Acta Mater. 53 (2005) 393–402.

[39] N. Hansen, Metall. Mater. Trans. A 32 (2001) 2917–2935.

[40] K. Edalati, T. Fujioka, Z. Horita, Mater. Sci. Eng. A 497 (2008) 168–173.

[41] H. Matsunaga, Z. Horita, Mater. Trans. 50 (2009) 1633–1637.

[42] L. Kurmanaeva, Y. Ivanisenko, J. Markmann, C. Kübel, A. Chuvilin, S. Doyle, R.Z. Valiev, H.J. Fecht, Mater. Sci. Eng. A 527 (2010) 1776–1783.

[43] Z.C. Duan, X.Z. Liao, M. Kawasaki, R.B. Figueiredo, T.G. Langdon, J. Mater. Sci. 45 (2010) 4621–4630.

[44] C. Xu, Z. Horita, T.G. Langdon, J. Mater. Sci. 43 (2008) 7286–7292.

[45] X.H. An, Q.Y. Lin, S.D. Wu, Z.F. Zhang, R.B. Figueiredo, N. Gao, T.G. Langdon, Philos. Mag. 91 (2011) 3307–3326.

[46] K. Edalati, Z. Horita, Mater. Sci. Eng. A 528 (2011) 7514–7523.

[47] Q.H. Tang, Y. Huang, Y.Y. Huang, X.Z. Liao, T.G. Langdon, P.Q. Dai, Mater. Lett. 151 (2015) 126–129.

[48] N.P. Li, The deformation of Vit1 bulk metallic glass under high pressure torsion Master's Dissertation, Yanshan University, 2012.

[49] N.V. Steenbergea, S. Hóbor, S. Surǐ nach, A. Zhilyaev, F. Houdellier, F. Mompiou, M.D. Baró, Á. Révész, J. Sort, J. Alloy. Compd. 500 (2010) 61–67.

[50] S. Lee, K. Edalati, Z. Horita, Mater. Trans. 51 (2010) 1072–1079 .

[51] V.K. Edalati, T. Fujioka, Z. Horita, Mater. Trans. 50 (2009) 44–50.

[52] K. Edalati, A. Yamamoto, Z. Horita, T. Ishihara, Scripta Mater. 64 (2011) 880–883.

[53] K. Edalati, E. Matsubara, Z. Horita, Metall, Mater. Trans. A 40 (2009) 2079–2085.

[54] K. Edalati, Z. Horita, S. Yagi, E. Matsubara, Mater. Sci. Eng. A 523 (2009) 277–281.

[55] K. Edalati, Z. Horita, Y. Mine, Mater. Sci. Eng. A 527 (2010) 2136–2141.

[56] M. Kawasakia, B. Ahn, T.G. Langdon, Mater. Sci. Eng. A 527 (2010) 7008–7016.

[57] R.J. Asaro, S. Suresh, Acta Mater. 53 (2005) 3369–3382.

[58] Z.S Ma, S.G Long, Y.C Zhou, Y. Pan, Scripta Mater. 59 (2008)195–198.

[59] T. Matsunaga, T. Kameyama, K. Takahashi, E. Sato, Mater. Trans. 50 (2009) 2865–2872.

Figure Captions

Fig. 1 XRD profiles of the HIPed $Al_{0.1}CoCrFeNi$ HEA and after HPT processing at 6 GPa for N = 1, 2, which indicate a single FCC structure.

Fig. 2 The upper row corresponds to optbical microstructures, and the lower row corresponds to the peripheries of the disks' TEM BF images with the associated SAED patterns of the HIPed $Al_{0.1}CoCrFeNi$ (a, d) and after HPT processing at 6 GPa for N = 1 (b, e) and 2 (c, f).

Fig. 3 Representative TEM BF micrographs of the $Al_{0.1}CoCrFeNi$ alloy after HPT at 6 GPa for N = 2. Planar slip of dislocations on {111}-type FCC planes is a dominant feature.

Fig. 4 TEM (a) BF image, (b) SAED pattern, (c) DF image, and (d) FFT-filtered image of HRTEM images of deformation twins for the sample processed under a pressure of 6 GPa after 2 revolutions. Twinning planes and twin boundaries are indicated by red and black straight lines, respectively.

Fig. 5 TEM of the secondary twin structures, primary twins running from top to bottom (red arrows), secondary twins in inclined orientations (blue arrows), BF image (a) and DF image (c); (b) SAED pattern indicated by {111} twinning; (d) HRTEM image showing the formation of twin junctions when secondary twins (blue lines) penetrate the primary twins (red lines).

Fig. 6 Vickers microhardness plotted against the distance from the center for the sample HIPed and HPT processed under a pressure of 6 GPa through 1 and 2 revolutions. Inset image illustrates the locations of hardness indents spaced 0.5

mm apart on the HPT disk.

Fig. 7 Typical load – displacement ($P - h$) curves from the center to the peripheries of the sample (6 GPa, $N = 2$). And r represents the distance of the test point to the center (a). Creep displacement versus time of the $Al_{0.1}CoCrFeNi$ alloy after HPT at 6 GPa for $N = 2$ (b).

Fig. 8 $\ln H$ versus $\ln t$ for the $Al_{0.1}CoCrFeNi$ alloy after HPT at 6 GPa for $N = 2$, crept at different positions.

Fig. 9 The microhardness variation of some pure metals and alloys processed by HPT. Hv_0 is the microhardness in the annealing state, and $\Delta Hv = Hv - Hv_0$, Hv is the saturation microhardness after being processed by HPT.

Figure 1

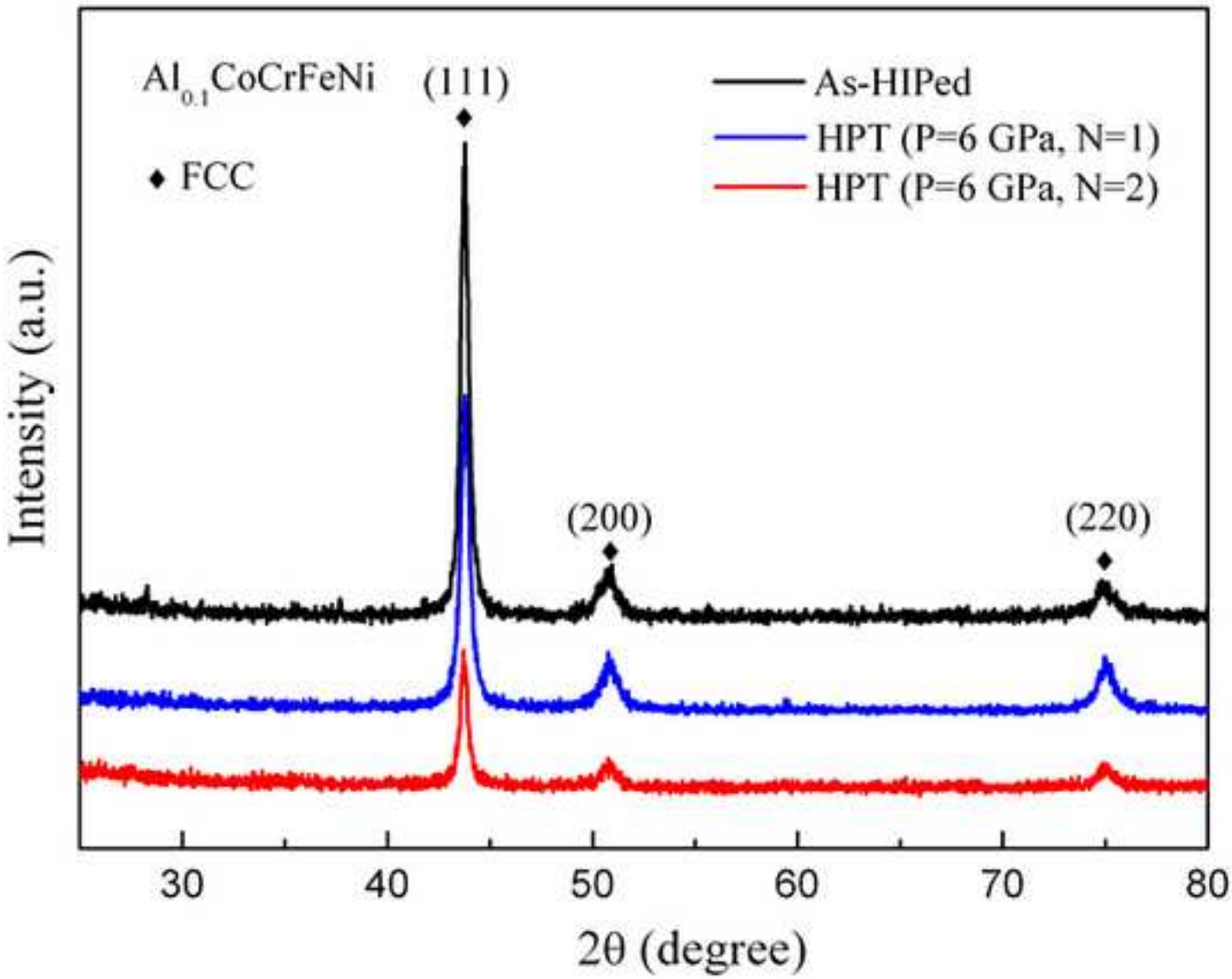
Al0.1CoCrFeNi
(111)
As-HIPed
HPT (P=6 GPa, N=1)
HPT (P=6 GPa, N=2)
FCC
(200)
(220)
Intensity (a.u.)
30
40
50
60
70
80
2θ (degree)

Figure 2

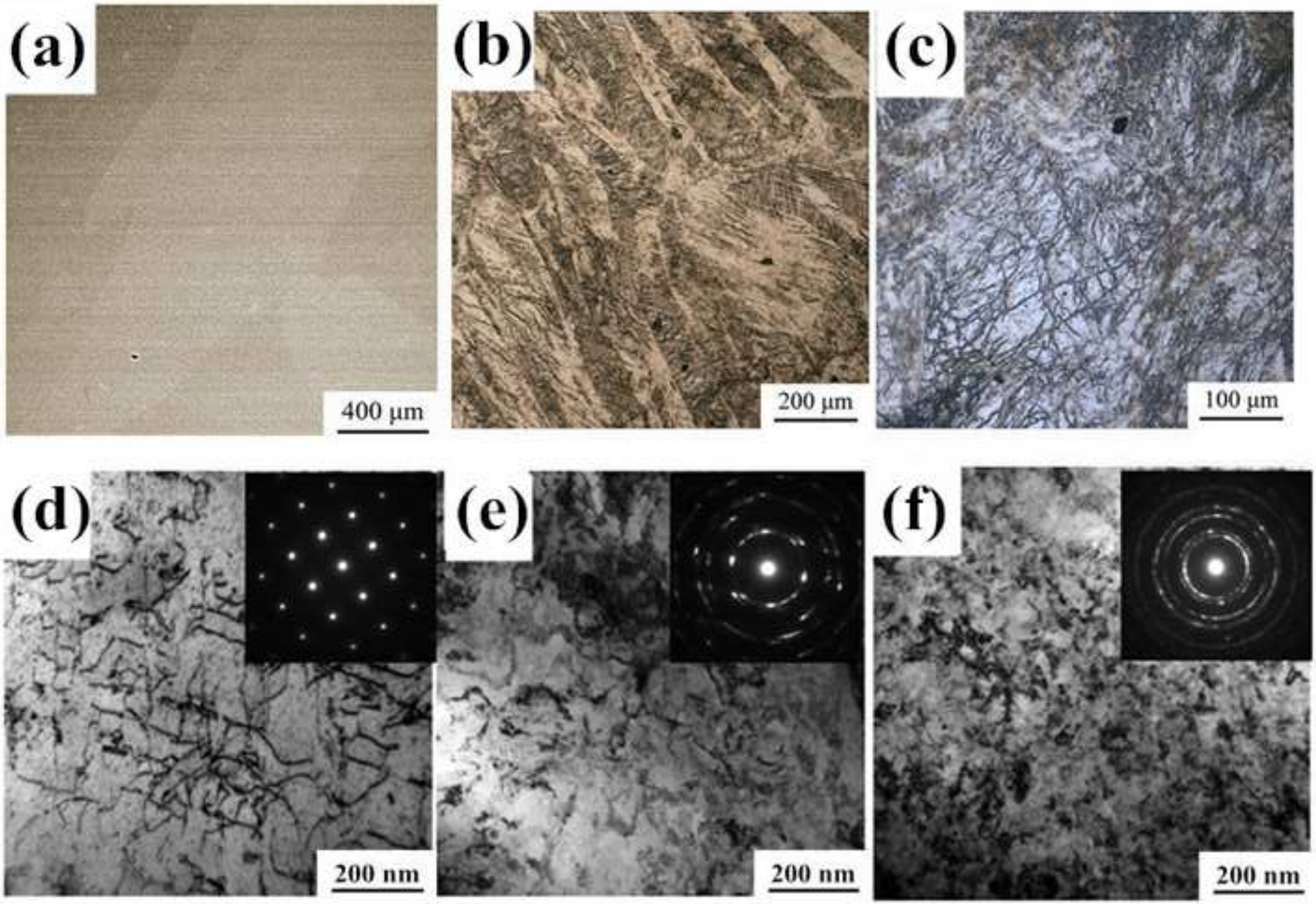

Figure 3

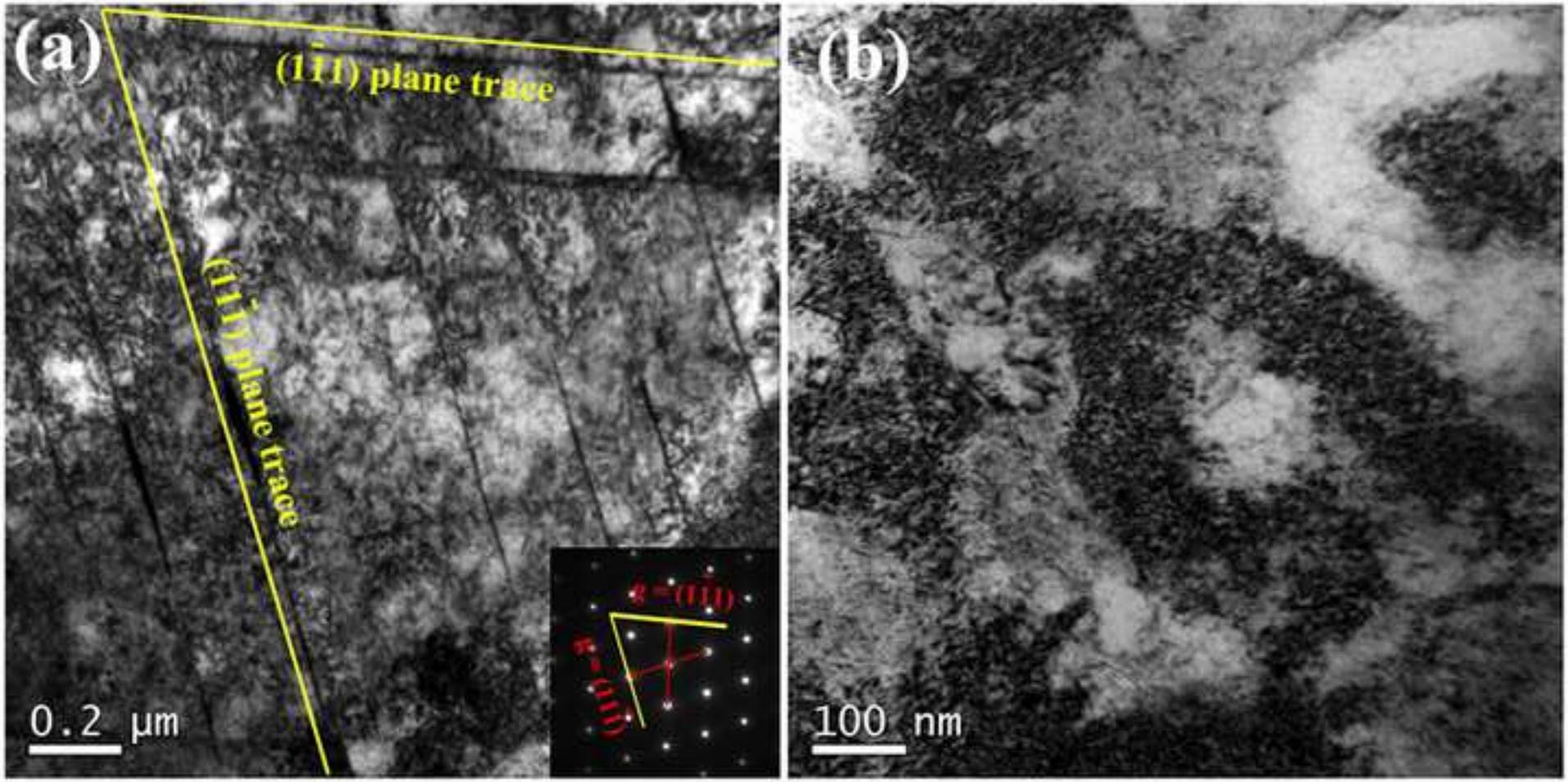

Figure 4

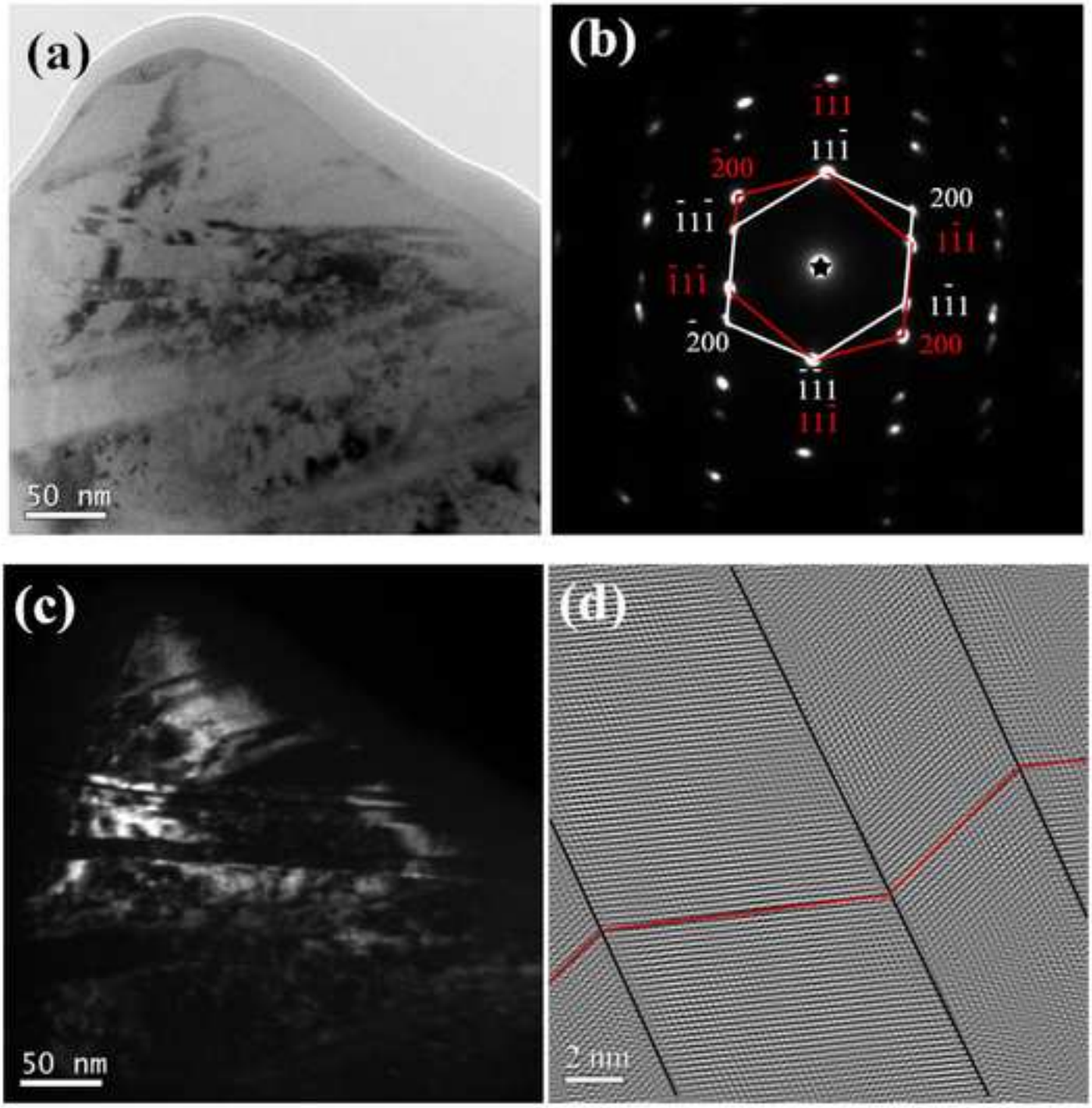
(a)
50 nm
(b)
$\bar{1}\bar{1}\bar{1}$
$1\bar{1}\bar{1}$
200
$\bar{2}00$
$\bar{1}\bar{1}1$
$\bar{1}1\bar{1}$
$\bar{1}11$
$\bar{2}00$
200
$11\bar{1}$
111
(c)
50 nm
(d)
2 nm

Figure 5

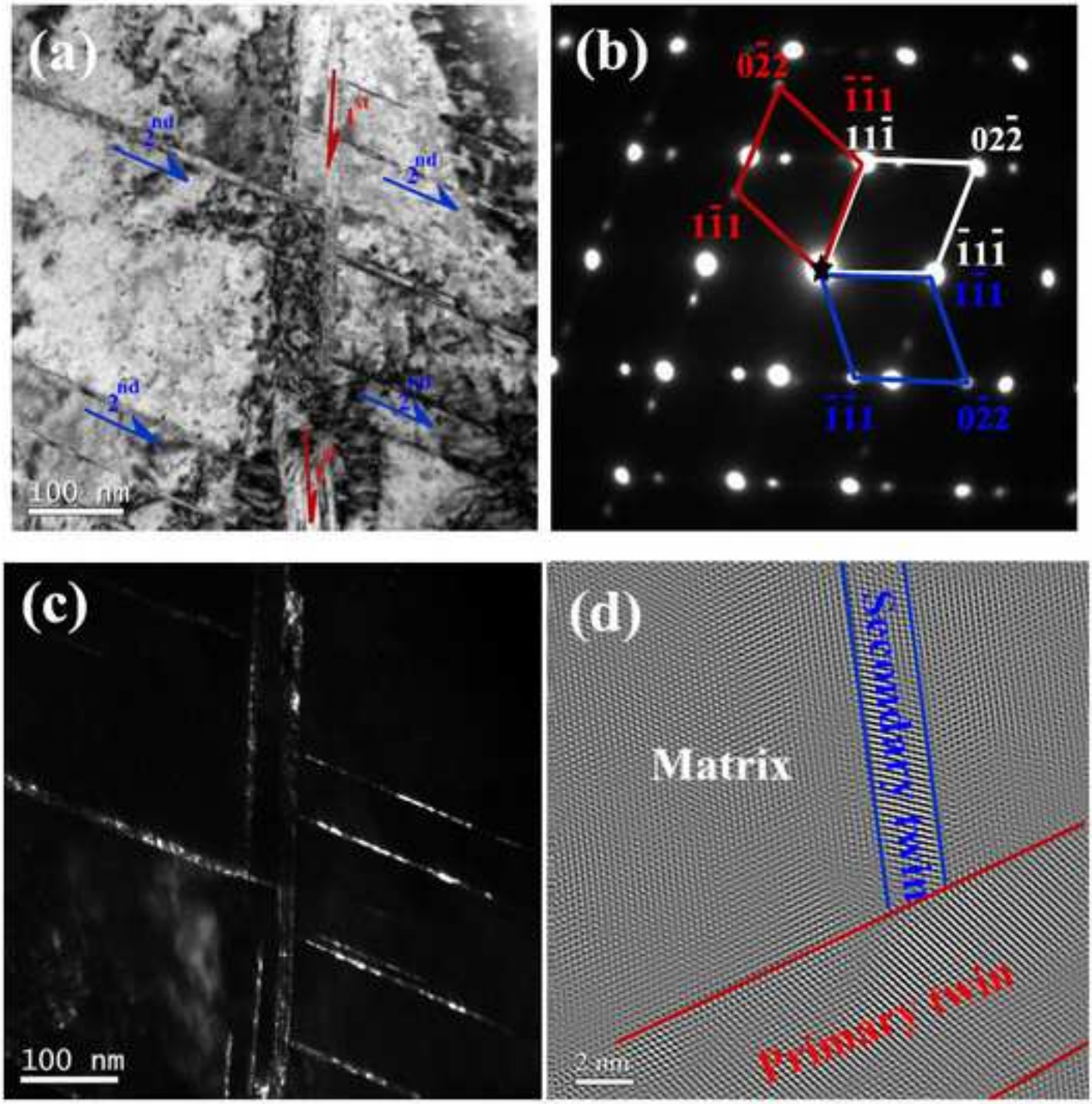
(a)
1st
2nd
2nd
2nd
2nd
100 nm
(b)
$0\bar{2}2$
$\bar{1}\bar{1}1$
$11\bar{1}$
$02\bar{2}$
$1\bar{1}1$
$\bar{1}11\bar{1}$
$\bar{1}\bar{1}\bar{1}$
$\bar{1}\bar{1}\bar{1}$
$02\bar{2}$
(c)
100 nm
(d)
Matrix
Secondary twin
Primary twin
2 nm

Figure 6

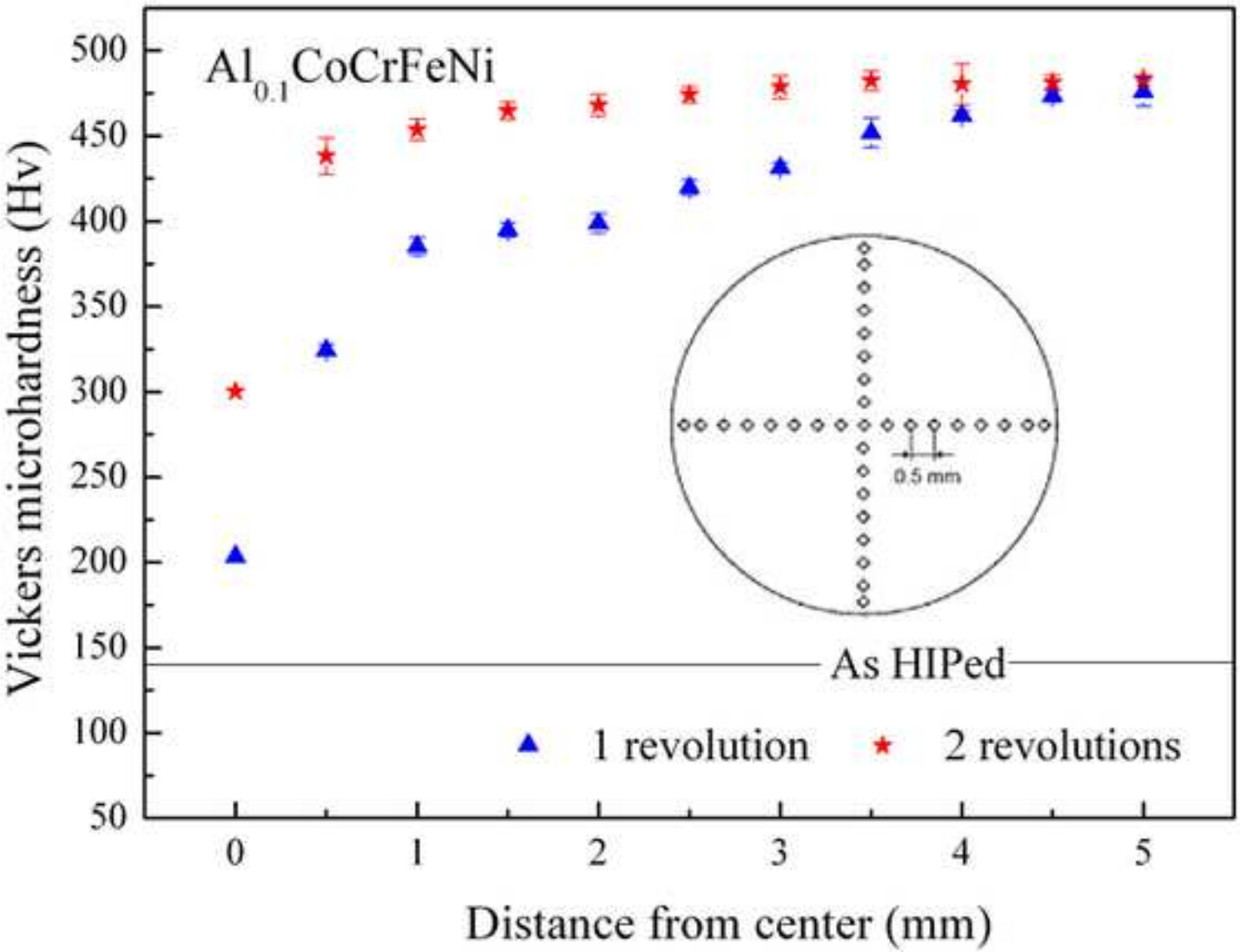
Al0.1CoCrFeNi
Vickers microhardness (Hv)
Distance from center (mm)
As HIPed
1 revolution
2 revolutions
0.5 mm
500
450
400
350
300
250
200
150
100
50
0
1
2
3
4
5

Figure 7

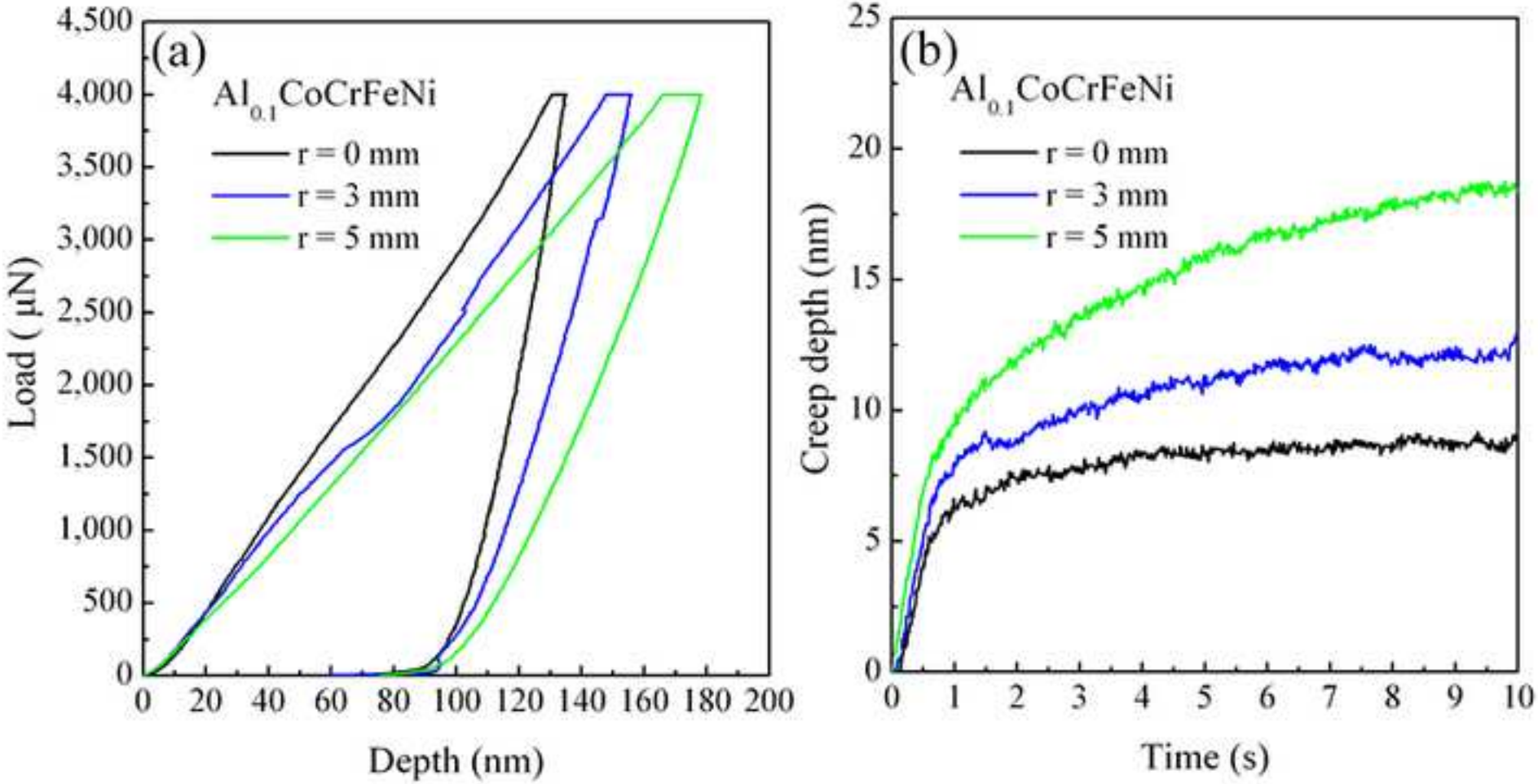
(a)
Al0.1CoCrFeNi
r = 0 mm
r = 3 mm
r = 5 mm
Load (μN)
Depth (nm)
4,500
4,000
3,500
3,000
2,500
2,000
1,500
1,000
500
0
0 20 40 60 80 100 120 140 160 180 200
(b)
Al0.1CoCrFeNi
r = 0 mm
r = 3 mm
r = 5 mm
Creep depth (nm)
Time (s)
25
20
15
10
5
0
0 1 2 3 4 5 6 7 8 9 10

Figure 8

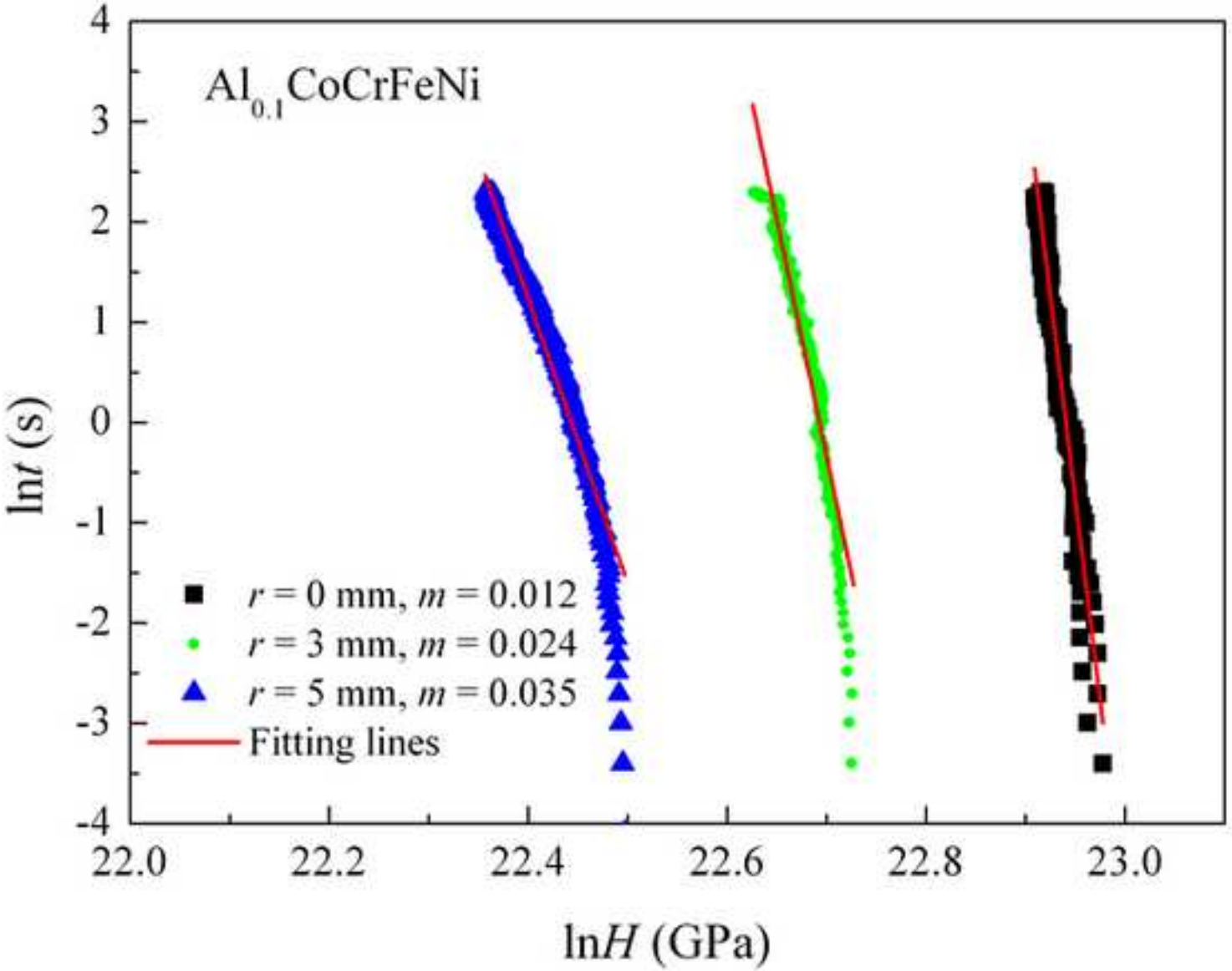
Al0.1CoCrFeNi
r = 0 mm, m = 0.012
r = 3 mm, m = 0.024
r = 5 mm, m = 0.035
Fitting lines
lnt (s)
lnH (GPa)
4
3
2
1
0
-1
-2
-3
-4
22.0
22.2
22.4
22.6
22.8
23.0

Figure 9

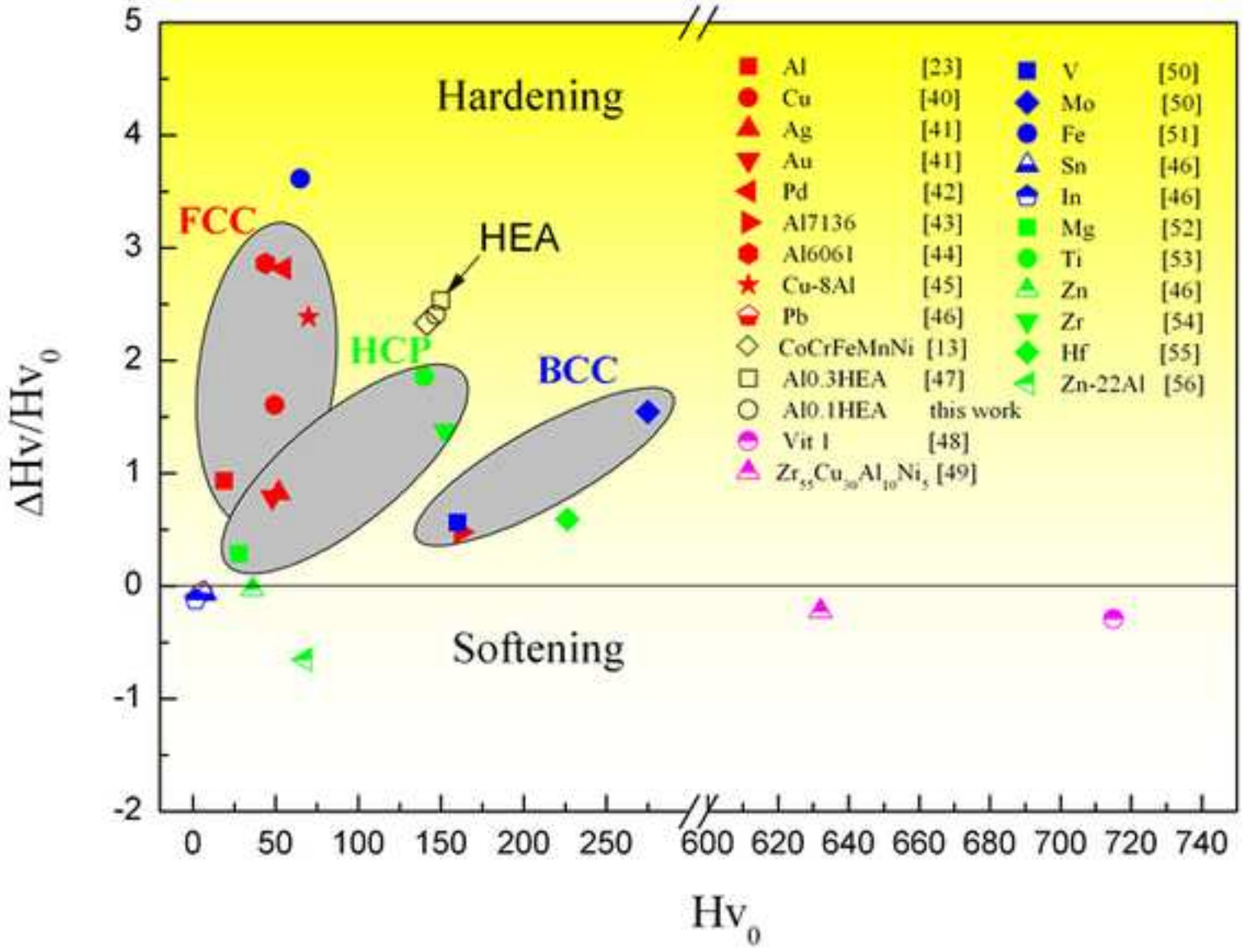
Hardening
Softening
FCC
HCP
BCC
HEA
Al [23]
Cu [40]
Ag [41]
Au [41]
Pd [42]
Al7136 [43]
Al6061 [44]
Cu-8Al [45]
Pb [46]
CoCrFeMnNi [13]
Al0.3HEA [47]
Al0.1HEA this work
Vit 1 [48]
Zr55Cu30Al10Ni5 [49]
V [50]
Mo [50]
Fe [51]
Sn [46]
In [46]
Mg [52]
Ti [53]
Zn [46]
Zr [54]
Hf [55]
Zn-22Al [56]
ΔHv/Hv0
Hv0
5
4
3
2
1
0
-1
-2
0
50
100
150
200
250
600
620
640
660
680
700
720
740